Supporting information file for

Momentum-Resolved Dielectric Response of Free-Standing Mono-, Bi- and Trilayer Black Phosphorus

Etienne Gaufrès[1,5]*, Frédéric Fossard[1], Vincent Gosselin[2], Lorenzo Sponza[1], François Ducastelle[1], Zhenglu Li[3,6], Steven G. Louie[3,6], Richard Martel[4], Michel Côté[2], and Annick Loiseau*[1]

[1] Laboratoire d'Etude des Microstructures, ONERA-CNRS, UMR104, Université Paris-Saclay, BP 72, 92322 Châtillon Cedex, France

[2] Département de physique, Université de Montréal, Montréal QC H3C 3J7, Canada

[3] Department of Physics, University of California at Berkeley, Berkeley, California 94720, USA

[4] Département de chimie, Université de Montréal, Montréal QC H3C 3J7, Canada

[5] Institut d'Optique & CNRS, LP2N UMR 5298, F-33400 Talence, France

[6] Materials Sciences Division, Lawrence Berkeley National Laboratory, Berkeley, California 94720, USA

*Correspondence to: annick.loiseau@onera.fr and etienne.gaufres@u-bordeaux.fr

Summary

1- Exfoliation and TEM grid preparation.

The TEM grids with BP were prepared in a glovebox with O_2 and H_2O partial pressure kept below 1ppm, as follows. The BP crystal (HQ graphene) was exfoliated using two slabs of PDMS. Then a TEM grid (copper, Holley carbon 300 mesh) is softly sandwiched between the two PDMS stamp to transfer some BP flakes on the grid. Then the grid is placed on double tilt TEM sample holder, previously inserted in the glove box. To avoid contamination and photooxidation of the flakes during the transfer to the TEM, the sample holder is sealed inside the glovebox by using a thermo-plastic bag. This bag wall is safely maintained on the TEM chamber hole and opened just before inserting the TEM sample holder.

2- Layer number determination based on HAADF Z-contrast.

2.1 Determination of the region-of-interest on a BP flake for EELS experiments

The presence of another flake or a change in thickness close to the probed area can strongly affect the EELS results. The Figure S0 presents an experiment, in witch a periodic recording of the EELS spectra along a line scan is performed, starting from vacuum, out of the flake to few nm inside the flake (aloof experiment). The spot-size of the electron beam is roughly 1.5-2 nm. As a results we observed that the electron beam senses the flake in the low loss regime until a distance of 15-20 nm from the flake, due to the electric field induced by the electron beam. We also noticed that the plasmon resonances are only excited when the beam is focused on the flake. In consequence we took a special care in positioning the beam probe at a minimum distance of 30 nm of another object, to avoid an eventual contamination of the loss signal.

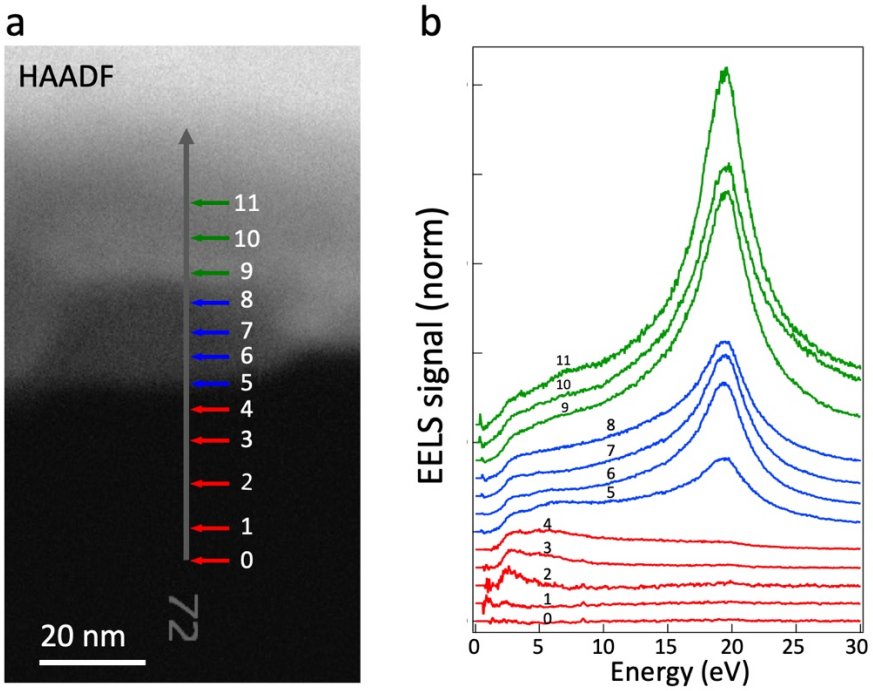

Figure S0: **a** HAADF image of a free-standing flake of BP exfoliated on TEM grid. The grey arrow indicates the line-scan direction. The coloured and numerated arrows point the positions of the beam positions for recording the EELS spectra displayed in panel (**b**). HAADF image and EELS spectra recorded at 80kV.

2.2 Analysis of the HAADF images for the layer number determination.

We have used the same calibration procedure that we used in the paper by Favron *et al* (Nature Materials (2015)). We have relied on the Z-contrast HAADF signal to measure the quantity of matter that interacts with the electron beam. Indeed, HAADF signals are directly related to the number of atoms and to the atomic number and the signal follows a power law, which makes it very sensitive to thickness. Further, the frequent observation of folded layers is very precious as it furnishes an internal calibration of the dependence of the HAADF intensity to the flake thickness. An example can be seen in Figure S1. A 3L part of the flake is folded (zone labelled 3L+3L) providing an internal thickness metrics.

In all cases, the zones selected for EELS measurements were at least over 100 nm in lateral size, so that they are solely illuminated by the electron beam both in EFTEM mode and in STEM mode for w-q mapping acquisition and that EELS signal is not polluted by proximity effect from the surrounding of the zone of interest.

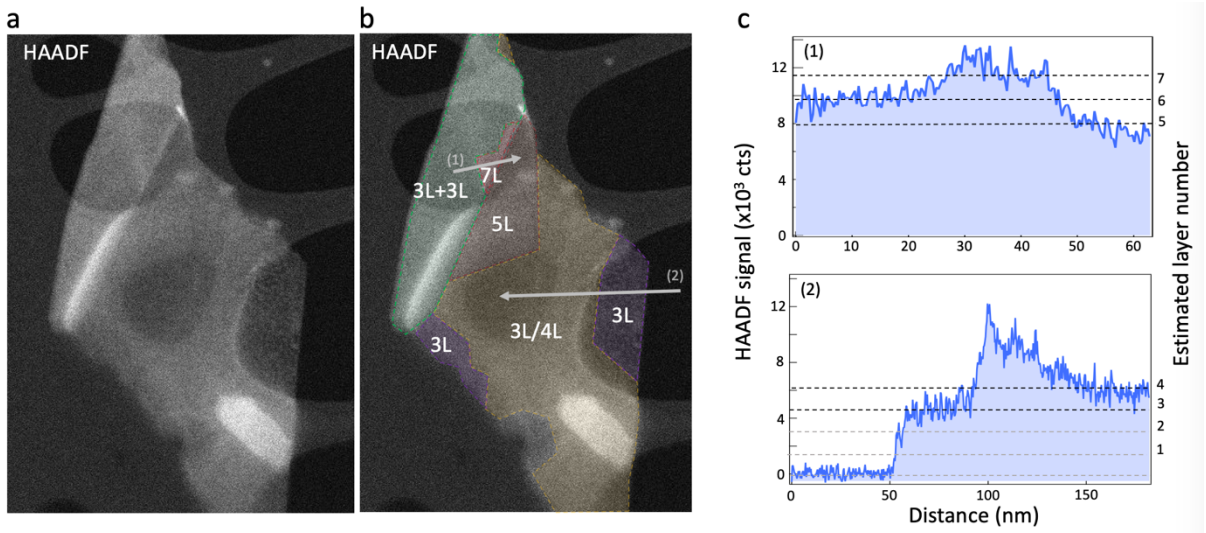

Figure S1. **a** HAADF image recorded at 80 kV of an exfoliated black phosphorus flake deposited on holey carbon TEM grids. b Same HAADF image as in **a** with a layer number indication using semi-transparent colour code based on the analysis of the HAADF profiles indicated by the numerated grey arrows and presented in panel **c**. The suspended trilayer was labelled trilayer 1 for the EELS experiment.

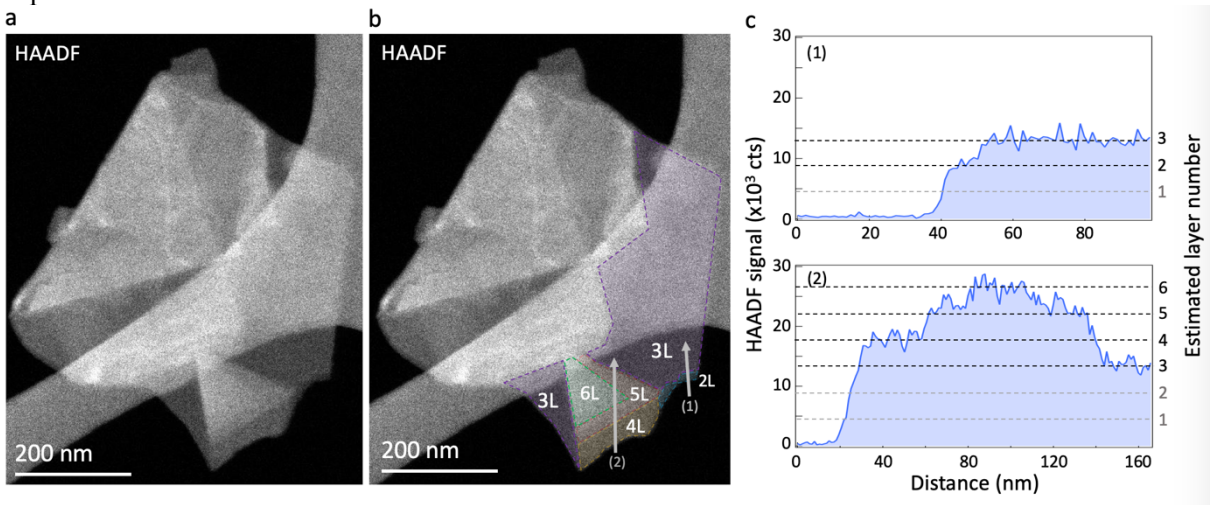

Figure S2. **a** HAADF image recorded at 80 kV of an exfoliated black phosphorus flake deposited on holey carbon TEM grids. b Same HAADF image as in **a** with a layer number indication using semi-transparent colour code based on the analysis of the HAADF profiles indicated by the numerated grey arrows and presented in panel **c**. The suspended trilayer was labelled trilayer 2 EELS experiment.

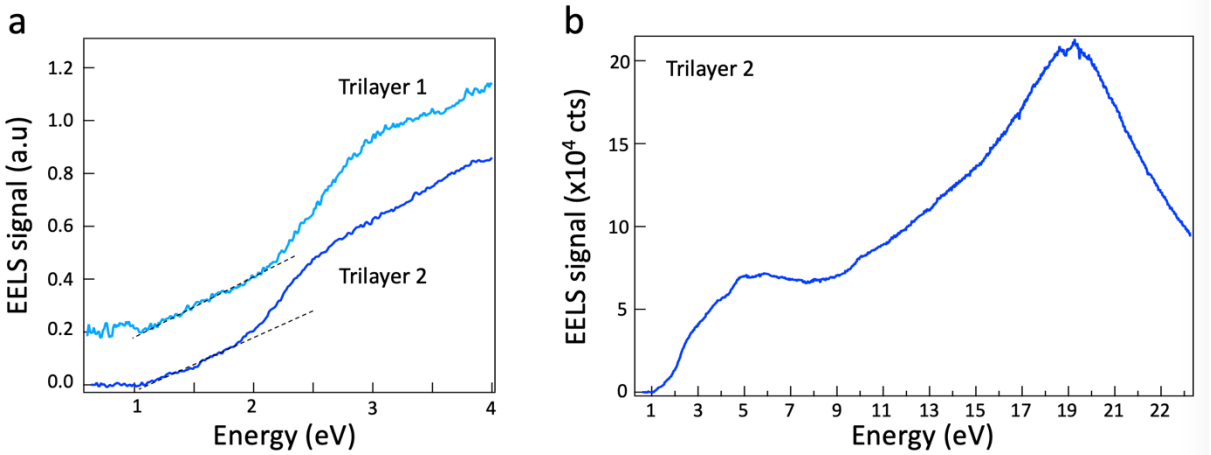

Figure S3. **a** EELS spectrum of trilayer 1 and trilayer 2 shown in Figures S1 and S2. from 0.6 eV to 4 eV. **b** EELS spectra of trilayer 2 recorded at 80kV from 0.6 eV to 22 eV. Spectra recorded at 80kV.

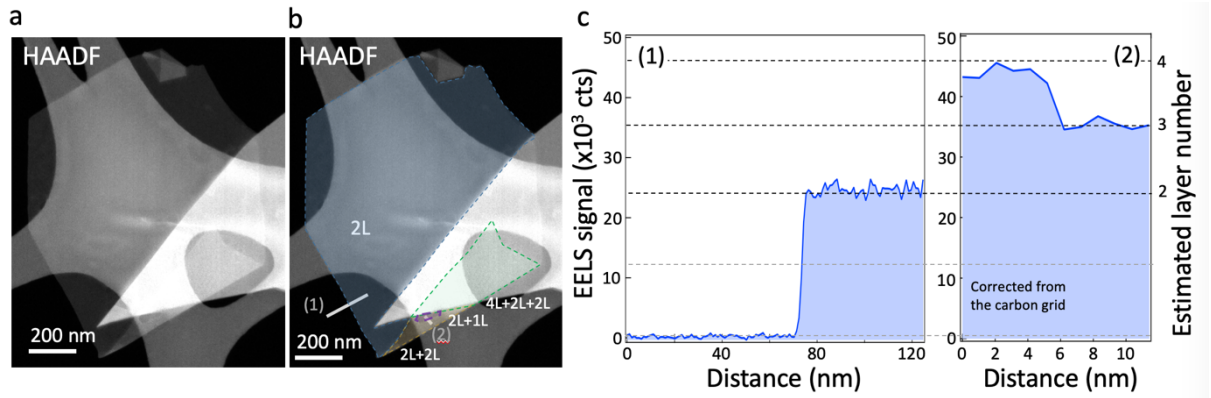

Figure S4. **a** HAADF image recorded at 80 kV of an exfoliated black phosphorus flake deposited on holey carbon TEM grids. b Same HAADF image as in **a** with a layer number indication using semi-transparent colour code based on the analysis of the HAADF profiles indicated by the numerated grey bars and presented in panel **c**. The suspended bilayer was labelled bilayer 1 for the EELS experiment.

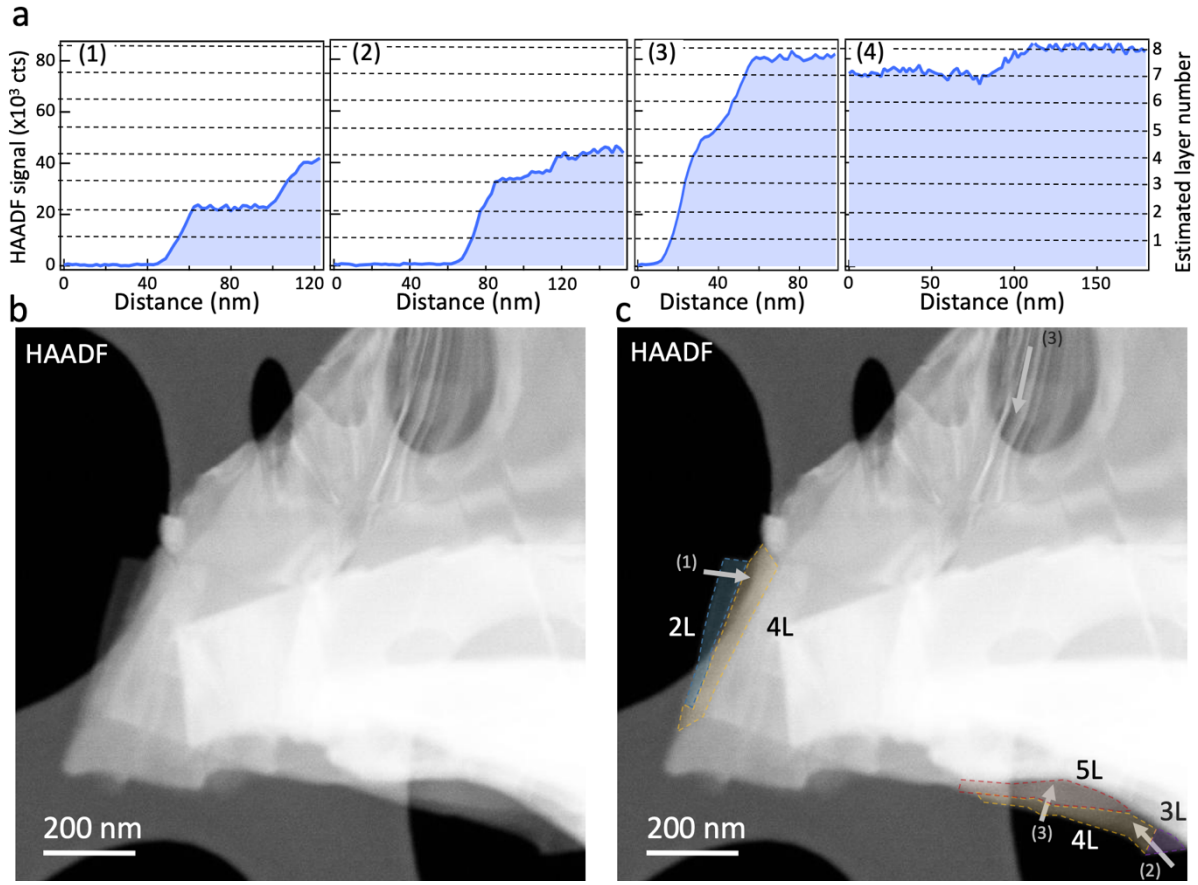

Figure S5. **a** HAADF image recorded at 80 kV of an exfoliated black phosphorus flake deposited on holey carbon TEM grids. b Same HAADF image as in **a** with a layer number indication using semi-transparent colour code based on the analysis of the HAADF profiles indicated by the numerated grey bars and presented in panel **c**. The suspended bilayer was labelled bilayer 2 for the EELS experiment.

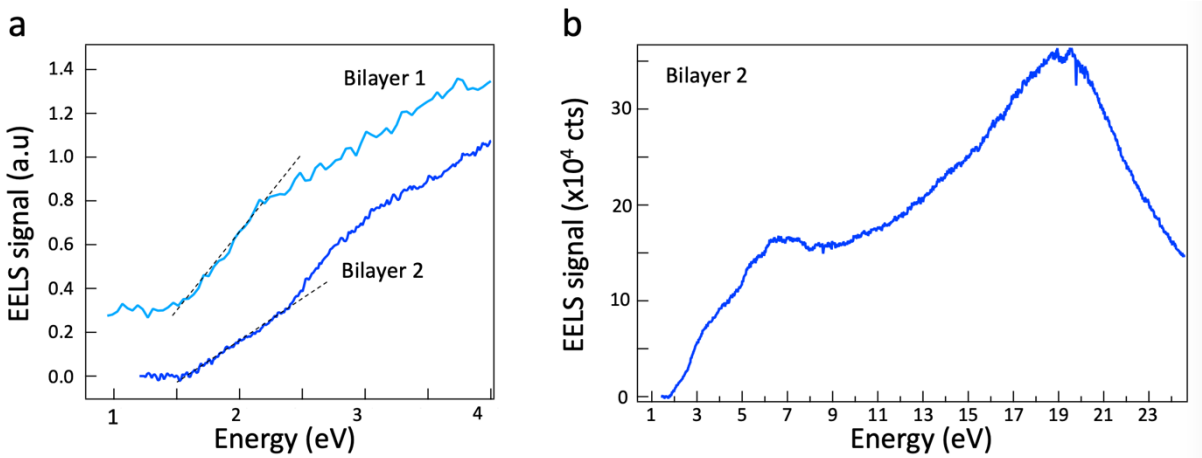

Figure S6. **a** EELS spectrum of bilayer 1 and bilayer 2 shown in Figures S1 and S2. from 0.6 eV to 4 eV. **b** EELS spectra of bilayer 2 recorded at 80kV from 1 eV to 24 eV. Spectra recorded at 80kV.

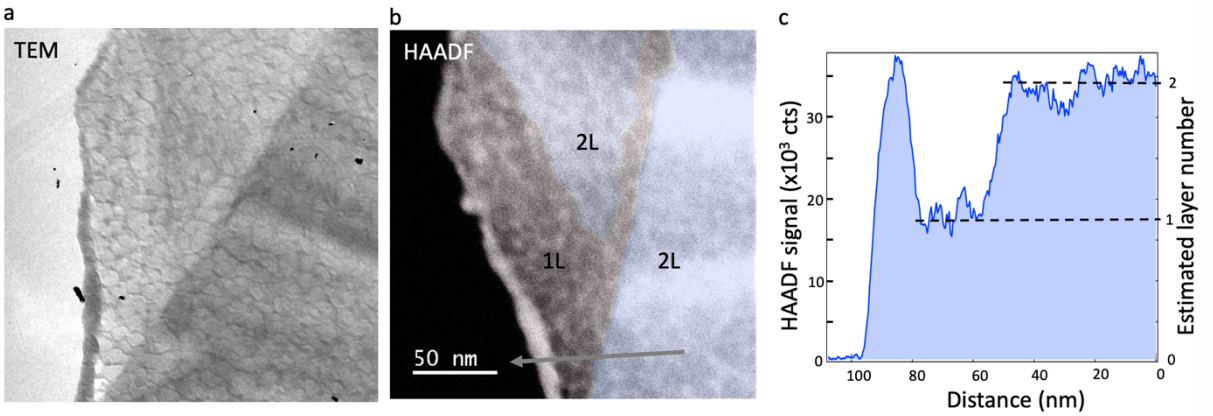

Figure S7. **a** TEM image recorded at 80 kV of an exfoliated black phosphorus flake deposited on holey carbon TEM grids. **b** HAADF image of the flake presented in **a** with a layer number indication using semi-transparent colour code based on the analysis of the HAADF profiles indicated by the numerated grey bars and presented in panel **c**. The suspended monolayer was labelled monolayer 1 for the EELS experiment.

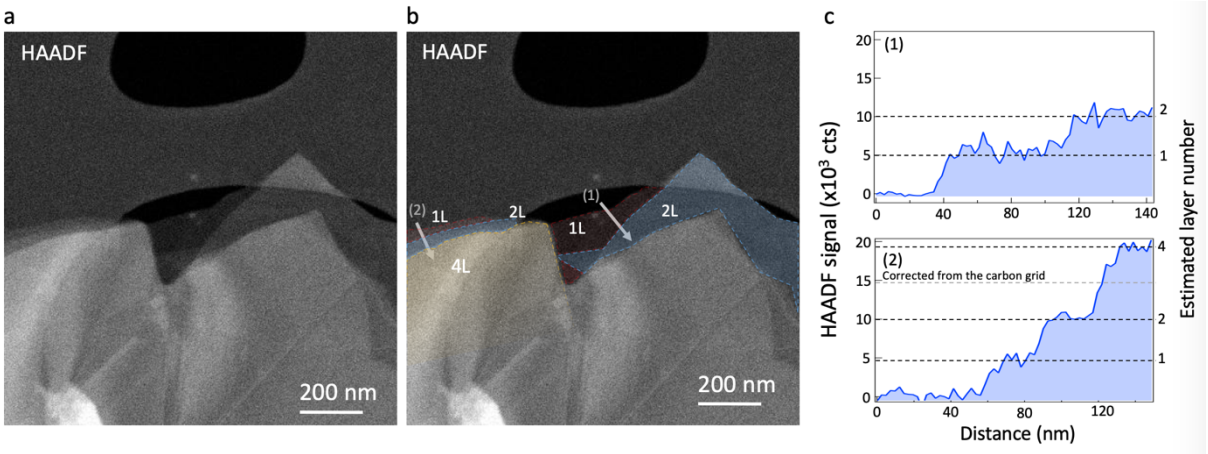

Figure S8. **a** HAADF image recorded at 80 kV of an exfoliated black phosphorus flake deposited on holey carbon TEM grids. b Same HAADF image as in **a** with a layer number indication using semi-transparent colour code based on the analysis of the HAADF profiles indicated by the numerated grey bars and presented in panel **c**. The suspended monolayer was labelled monolayer 2 for the EELS experiment.

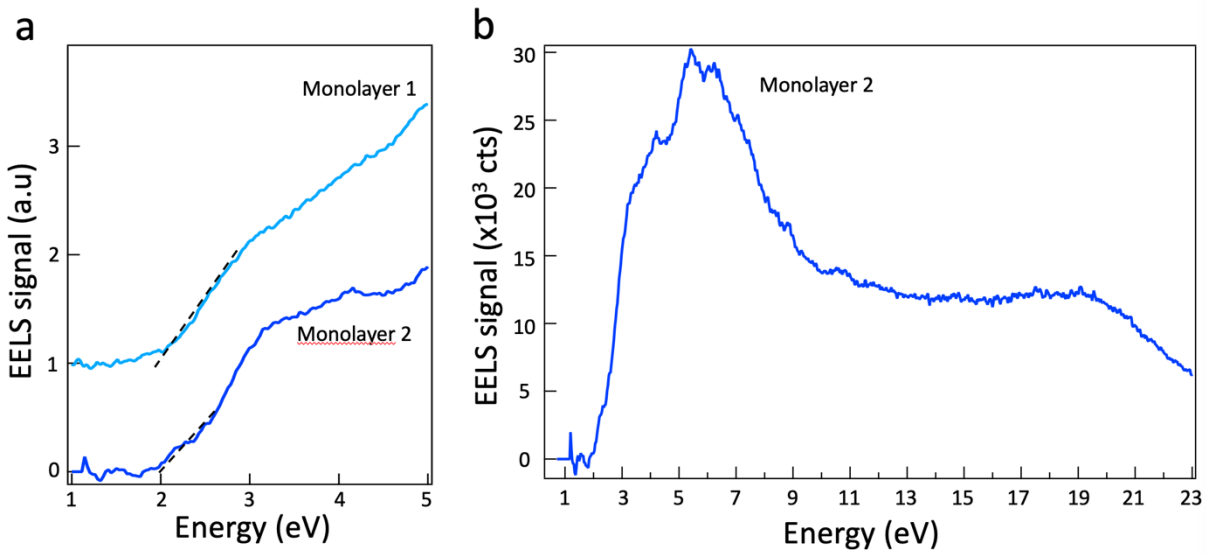

Figure S9. **a** EELS spectrum of monolayer 1 and monolayer 2 shown in Figures S1 and S2. from 0.6 eV to 4 eV. **b** EELS spectra of monolayer 2 recorded at 80kV from 0.6 eV to 23 eV. Spectra recorded at 80kV.

Table S1. Threshold values extracted from EELS spectra of mono, bi, trilayer BP presented in Figures S3, S6, S9.

BP Sample	**Near band edge threshold (eV)**	**Error (eV)**
Monolayer #1	1.9	0.1
Monolayer #2	2.0	0.1
Bilayer #1	1.4	0.1
Bilayer #2	1.5	0.1
Trilayer #1	1.1	0.15
Trilayer #2	1.1	0.15

3- Computational details (gap and binding energy)

The three free-standing structures have been relaxed with the ABINIT plane-wave code, using Troullier-Martins pseudopotentials. The Brillouin zone has been sampled with a 9x1x7 Γ-centred k-point grid, with a cut-off energy 40 Ha and the PBE approximation to the exchange-correlation potential. The tolerance in the stress tensor during structural optimization has been set to 0.0001 Ha/Bohr (~0.0007 eV/Å) per component per atom. The resulting structural parameters are summarized in Table S1.

Table S1:

	Monolayer	Bilayer	Trilayer
zigzag a (Å)	3.281	3.284	3.286
armchair c (Å)	4.609	4.579	4.571
thickness h (Å)	2.090	7.726	13.377

Once the equilibrium structure has been obtained, the Kohn-Sham Hamiltonian has been diagonalized with the GPAW code, using a cutoff energy of 700 eV (a new convergence in the cutoff was needed because GPAW uses a PAW basis). In all cases, the Coulomb truncation method has been employed and 10 Å of vacuum have been included in each simulation cell.

The Bethe-Salpeter equation (BSE) has been solved using the GPAW code, using a cutoff energy of 50 eV and a broadening constant of 0.05 eV. The other parameters of the BSE calculation and the value of the scissor operator are summarized in Table 2.

Table 2:

	Monolayer	Bilayer	Trilayer
N. bands in ε	40	80	120
N. valence bands	3	6	9
N. conduction bands	4	8	12
k-point grid (Γ-centred)	31x1x25	31x1x25	25x1x17
cell height L=V+h (Å)	12.11	17.73	23.38
Scissor operator (eV)	1.56	1.31	1.03

The scissor operator has been fixed in such a way that the optical gap extracted from the simulated loss function matches the EELS measurements of this work. This leads to fundamental gaps of 2.46 eV, 1.90 eV and 1.34 eV in the 1-, 2- and 3-layer systems respectively. The value of the monolayer compares well with the most advanced calculations found in literature (2.4 eV obtained with Monte Carlo Methods[1] and 2.41 eV obtained with GW0+hybrid[2,3]).

The choice of vacuum in BSE calculations

It is known that simulations of isolated systems in the reciprocal space are affected by errors due to the implicit assumption of periodic boundary conditions. The introduction of an appropriately truncated Coulomb potential cures this issue permitting in addition to reduce a lot the unavoidable empty space. However, since the RPA polarizability is renormalized with respect to the volume of the cell, some arbitrariness remains in choosing how much vacuum has to be included, despite the use of the Coulomb truncation. As we show below this has severe consequences on the BSE calculation.

In Figure S1 we report test BSE spectra (not all parameters are at convergence) of the BP monolayer done with the Coulomb truncation in six cells differing by the amount of vacuum *V*. As it can be seen, despite the use of the Coulomb truncation, the first peak Ex is continuously blue-shifted as *V* is decreased, without exhibiting any convergence trend. This is highlighted in the inset by the green line, which reports Ex(1/L) in arbitrary units (L=V+h is the height of the simulation cell).

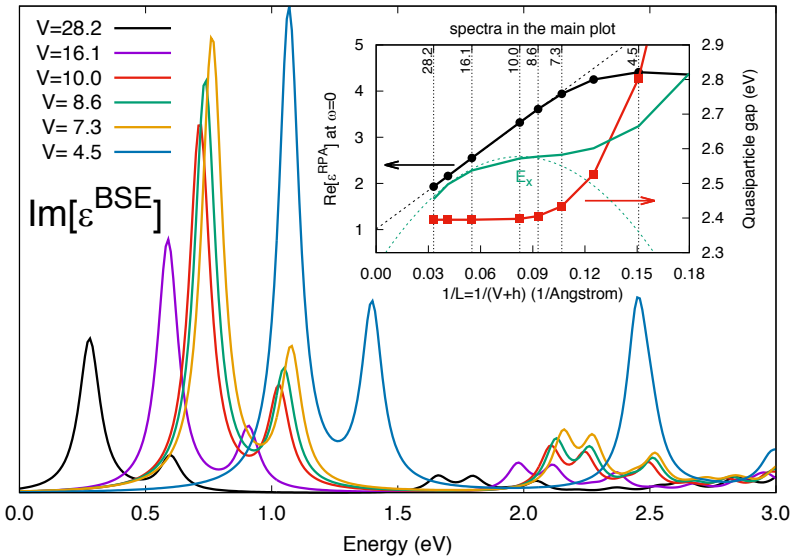

Figure S2: Body: Shift of the excitonic peak E_x in a generic 2D material (in this case a test calculation of BP monolayer) as function of the vacuum *V* included in the simulation cell. Inset: the fundamental gap $E_g(1/L)$ in red, the dielectric function $\varepsilon(1/L)$ in black and the trajectory of the excitonic peak $E_x(1/L)$ expressed in arbitrary units in green. L=V+h is the total height of the simulation cell. Lengths are in Angstrom, energies in eV.

To understand this behaviour and to specify a criterion to fix V, we have considered the variation of the dielectric function ε and of the gap E_g as function of 1/L, reported in the inset of Figure S2. Let us first focus on the black curve, the dielectric function $\varepsilon(1/L)$. For large enough cells, the dielectric function is expected to follow the linear law $\varepsilon(1/L) = 1 + 4\pi\alpha/L$ with α being the slab polarizability.[4,5] With no surprises, this is confirmed in our calculations. This means that for high-enough V, the screening entering the BSE calculation is very weak. However, in small cells (in our case starting from L=7.3 Å) the dielectric function starts deviating from the linear law bending to lower values. This is due to an artificial confinement of the electronic wave functions, as attested by the sudden increase of $E_g(1/L)$ (the fundamental gap, red curve) which instead is stable in large cells.

Combining these two elements, the continuous blue-shift of Ex can be easily explained. If too much empty space is included in the cell, the gap is at convergence, but the dielectric screening is too weak, leading to high binding energies and hence to low-energy excitons. Instead, when not enough vacuum is included, the artificially high confinement opens the gap too much and even if the exciton binding energy increases ($\varepsilon(1/L)$ bends downward), the effect does not compensate the band gap opening.

One can define the optimum vacuum V' as the amount such that $E_g(1/L)$ is converged and the linear law of the dielectric function $\varepsilon(1/L)$ still holds. In our case V'=10 Å. Because of the arguments invoked, we don't expect this value to change in the bilayer and the trilayer cases.

Anisotropic variational model of the exciton binding energy

Prada and co-workers derived a variational model for excitons in an anisotropic free-standing slab.[6]The model, based on a Wannier-Mott picture and strongly inspired by the pioneering work of Keldysh[7], provides estimations of the exciton binding energy and of the average electron-hole distance in the two directions of anisotropy. We generalised the model to take into account the effects of two sandwiching dielectrics characterised by dielectric functions ε_1 and ε_2 as in the original problem addressed by Keldysh.[7] The environment enters then in the equations through an average dielectric function $\varepsilon=(\varepsilon_1+ \varepsilon_2)/2$.

The electron-hole pair is characterised by two parameters: the effective mass μ that we obtained from our DFT calculations, and a typical screening distance $r_0 = r_0^{FS}/\varepsilon$ where r_0^{FS} is the corresponding parameter in the free-standing case. In the 1-, 2- and 3-layer we set r_0^{FS} in such a way to reproduce the binding energy predicted by our BSE simulations.

In Table 3, we report the parameter r_0 used, together with the predicted excitonic radii (a_x and a_z), and the binding energies E_b for several environmental conditions found in literature. The corresponding optical gap E_x reported in Table 3 are obtained by subtracting the simulated E_b to the measured E_g (see also main text).

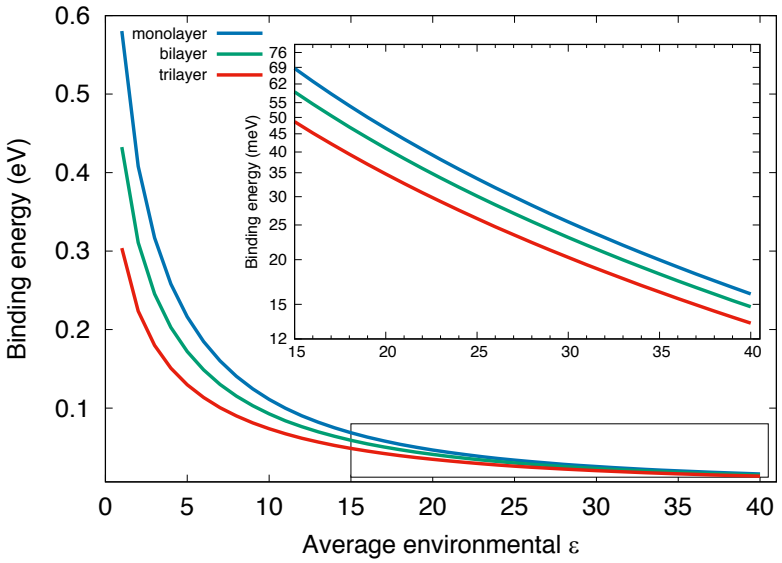

Figure S3: Variation of the binding energy E_b as function of the average dielectric function of the surroundings. Results have been obtained with the variational model.

Table S3: Results of the variational model in different environments, and comparison with experiments.[8-12] Distances are in Bohr, energies in eV. References in the Table are [14, 15, 16, 20, 21].

	$\bar{r}_0$	a_x	a_z	E_b	E_X (exp.)	E_g
$\bar{\epsilon} = 46.7$ **Liquid solvent (DMF)** (8):						
monolayer	1.99	25.09	71.49	-0.01	1.35	1.36
bilayer	2.89	27.68	75.29	-0.01	1.24	1.25
trilayer	4.50	30.61	79.07	-0.01	1.04	1.05
$\bar{\epsilon} = 36.7$ **Liquid solvent (DMSO)** (8):						
monolayer	2.53	21.07	59.58	-0.02	1.38	1.40
bilayer	3.68	23.38	62.73	-0.02	1.23	1.25
trilayer	5.72	26.32	67.20	-0.02	1.06	1.08
$\bar{\epsilon} = 32.17$ **Liquid solvent (NMP)** (9):						
monolayer	2.89	19.28	54.24	-0.02	—	—
bilayer	4.20	21.51	57.55	-0.02	1.88	1.90
trilayer	6.53	24.41	62.22	-0.02	1.43	1.45
$\bar{\epsilon} = 8.28$ **Saphire + hBN** (10):						
monolayer	11.23	10.32	27.10	-0.14	1.73	1.87
bilayer	16.30	12.28	30.72	-0.11	1.15	1.26
trilayer	25.36	15.03	35.93	-0.09	0.85	0.94
$\bar{\epsilon} = 7.0$ **Liquid solvent (CHP)** (11):						
monolayer	13.29	9.88	25.76	-0.16	1.97	2.13
bilayer	19.29	11.83	29.38	-0.13	1.33	1.46
trilayer	30.00	14.57	34.62	-0.10	1.14	1.24
$\bar{\epsilon} = 2.3$ **SiO_2** (12):						
monolayer	40.43	8.31	20.84	-0.38	1.75	2.13
bilayer	58.70	10.18	24.47	-0.29	1.29	1.58
trilayer	91.30	12.86	29.87	-0.21	0.97	1.18
$\bar{\epsilon} = 1.0$ **Free standing**:						
monolayer	93.00	7.86	19.42	-0.58	1.88	2.46
bilayer	135.00	9.70	23.04	-0.43	1.47	1.90
trilayer	210.00	12.34	28.24	-0.30	1.04	1.34

Note concerning the electronic gap calculation.

It should be stressed once more that, since it has been fixed *a posteriori* to reproduce the EELS threshold, the value of 2.4 is essentially an experimental measure. Indeed, we have used ab-initio methods more as a powerful analysis tool, than in virtue of their predictive power. Therefore, in comparing our results to other purely theoretical values reported in literature, one should avoid speculating on the reasons of possible differences, while take instead our result as an "experimental benchmark" against which theoretical methods should be tested. In this sense, our findings are consistent with the theoretical simulations of the electronic gap in the free-standing monolayer. Theoretical values range from 1.6 eV to 2.4 eV, depending on the approximations, but the two most advanced methods (Monte Carlo and

hybrid+GW_0) give both a fundamental gap of 2.4 eV (see Frank *et al.*[1] and references therein), in very good agreement with our findings.

References

(1) Frank, T.; Derian, R.; Tokár, K.; Mitas, L.; Fabian, J.; Štich. I. Many-Body Quantum Monte Carlo Study of 2D Materials: Cohesion and Band Gap in Single-Layer Phosphorene. *Phys. Rev. X* **2019,** 9, 011018

(2) Wang, V.; Kawazoe, Y.; Geng, W. T. Native point defects in few-layer phosphorene. *Phys. Rev. B* **2015,** *91,* 045433

(3) Qiu, D.; da Jornada, F. H.; Louie, S. G. Environmental Screening Effects in 2D Materials: Renormalization of the Bandgap, Electronic Structure, and Optical Spectra of Few-Layer Black Phosphorus. *Nano Lett*. **2017,** 17, 4706

(4) Cudazzo, P.; Tokatly, I. V.; Rubio, A. Dielectric screening in two-dimensional insulators: Implications for excitonic and impurity states in graphane. *Phys. Rev. B* **2011**, 84, 085406

(5) Sponza, L.; Goniakowski, J.; Noguera, C. Confinement effects in ultrathin ZnO polymorph films: Electronic and optical properties. *Phys. Rev. B* **2016**, 93, 195435

(6) Prada, E.; Alvarez, J. V.; Narasimha-Acharya, K. L.; Bailen F. J.; Palacios, J. J. Effective-mass theory for the anisotropic exciton in two-dimensional crystals: Application to phosphorene. *Phys. Rev. B* **2015**, 91, 245421

(7) Keldysh, L. V. Coulomb interaction in thin semiconductor and semimetal films *JETP Lett*. **1978**, 29, 658

(8) Yasaei, P.; Kumar, B.; Foroozan, T.; Wang, C.; Asadi, M.; Tuschel, D.; Indacochea, J. E.; Klie, R. F.; Salehi-Khojin, A. High-Quality Black Phosphorus Atomic Layers by Liquid-Phase Exfoliation. *Adv. Mater.* **2015**, 27, 1887

(9) Woomer, A. H.; Farnsworth, T. W.; Hu, J.; Wells, R. A.; Donley, C. L.; Warren, S. C. Phosphorene: Synthesis, Scale-Up, and Quantitative Optical Spectroscopy. *ACS Nano* **2015**, 9, 8869

(10) Li, L.; Kim, J.; Jin, C.; Ye, G. J.; Qiu, D. Y.; da Jornada, F. H.; Shi, Z.; Chen, L.; Zhang, Z.; Yang, F.; Watanabe, K.; Taniguchi, T.; Ren, W.; Louie, S. G; Chen, X. H.; Zhang, Y.; Wang, F. Direct observation of the layer-dependent electronic structure in phosphorene. *Nat. Nanotech*. **2016**, 12, 21

(11) Hanlon, D.; Backes, C; Doherty, E.; Cucinotta, C. S.; Berner, N. C; Boland, C.; Lee, K.; Harvey, A; Lynch, P; Gholamwand, Z.; Zhang, S.; Wang, K; Moynihan, G; Pokle, A; Ramasse, Q. M.; McEvoy, N.; Blau, W. J.; Wang, J.; Abellan, G.; Hauke, F; Hirsh, A; Sanvito, S.; O'Regan, D. D; Duesberg, G. S; Nicolosi, V; Coleman, J. N. Liquid exfoliation of solvent-stabilized few-layer black phosphorus for applications beyond electronics. *Nature Comm*. **2015**, 6, 8563

[12] Yang, J.; Xu, R.; Pei, J.; Myint, Y. W; Wang, F; Wang, Z.; Yu, Z.; Lu, Y. Unambiguous identification of monolayer phosphorene by phase-shifting interferometry. *ArXiv* **2014**, 1412:6701